ACS APPLIED MATERIALS & INTERFACES

Research Article

www.acsami.org

Tuning Solid-State Fluorescence to the Near-Infrared: A Combinatorial Approach to Discovering Molecular Nanoprobes for Biomedical Imaging

Ajay Singh,[†,‡,§] Chang-Keun Lim,[†,§] Yong-Deok Lee,[†] Joon-ho Maeng,[†] Sangyoup Lee,[†] Joonseok Koh,*[,‡] and Sehoon Kim*[,†]

[†]Center for Theragnosis, Korea Institute of Science and Technology, 39-1 Hawolgok-dong, Seongbuk-gu, Seoul 136-791, Korea

[‡]Department of Textile Engineering, Konkuk University, Seoul 143-701, Korea

Supporting Information

ABSTRACT: Dyes showing solid-state fluorescence (SSF) are intriguing molecules that can emit bright fluorescence in the condensed phase. Because they do not suffer from self-quenching of fluorescence, nanoscopic dense integration of those molecules produces particulate nanoprobes whose emission intensity can be boosted by raising the intraparticle dye density. In spite of the potential promise for imaging applications demanding intense emission signals, their excitation and emission spectra are generally limited to the visible region where biological tissues have less transparency. Therefore, the SSF-based nanoprobes have rarely been applied to noninvasive in vivo imaging. Here we report a combinatorial chemistry approach to attain a high level of tissue transparency of SSF by tuning its excitation and emission wavelengths to the truly near-infrared (NIR) region. We built a dipolar arylvinyl (ArV) scaffold-based chemical library where the optical bandgap could be narrowed to the NIR above 700 nm by combinatorial modulation of the π-electron push-pull strengths. The ArV-aggregated nanoparticles (FArV NPs) with a colloidal size less than 20 nm were formulated using a polymeric surfactant (Pluronic F-127) and applied to bioimaging in cells and in vivo. We demonstrate that some of FArV NPs have truly NIR excitation and emission of SSF, capable of noninvasive in vivo imaging (efficient lymph node mapping and early diagnosis of tumor) in mouse models by virtue of bright solid-state NIR fluorescence and high signal-to-background contrast (S/B $\approx$ 8) as well as facile circulation in the living body.

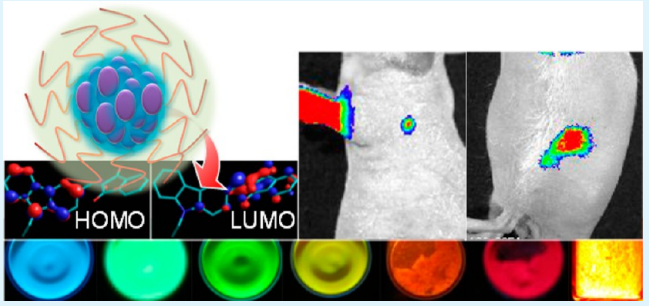

KEYWORDS: *aggregation-enhanced fluorescence, biomedical in vivo imaging, combinatorial chemistry, dye-concentrated nanoparticles, solid-state NIR fluorescence*

Molecular fluorescence has led to great leaps in biological and biomedical research, because of the high sensitivity, easy accessibility, multi-parametric detectability, and availability of diverse natural and synthetic fluorescent molecules.[1,2] Recently, organic nanoparticles composed of molecular aggregates that emit solid-state fluorescence (SSF) or aggregation-enhanced fluorescence (AEF) have been gaining great interest as a newly emerging class of molecule-integrated fluorescent nanoprobes because of their potential promise for bioimaging applications demanding intense emission signals.[3−12] SSF is a unique phenomenon that can keep the fluorescing capability in the concentrated or aggregated states to overcome typical fluorescence quenching of common organic dyes. It allows for high-density loading of dyes in the particle interior, to provide dye-aggregated molecular nanoprobes whose emission intensity is boosted proportional to the loading density. Furthermore, dye aggregation into nanoparticles makes it easy to produce a water-dispersed formulation of dyes for biomedical uses, without necessity of chemical modification for water solubilization. Nanoparticle formulation may offer additional advantages including enhanced cell permeability, passive in vivo tumor targeting by the enhanced permeability and retention (EPR) effect, and surface engineering by multiple bioconjugation for active targeting.[13,14]

In general, SSF occurs in a special class of molecules showing AEF. In most cases, they have nonplanar geometries with torsional freedom that cause fluorescence quenching in the isolated solution state, whereas their emission shows great enhancement upon blocking the torsional motion by solidification.[15−20] Various kinds of AEF-active dyes with a wide spectral range of emission have successfully been applied to bioimaging and sensing applications. However, most of them show emission in the visible window below 650 nm; SSF in the near-infrared (NIR) has rarely been reported to date.[8−12] For biomedical in vivo imaging, spectral tuning to the NIR is demanded because the NIR region has the deepest light penetration into biological tissues with less photon-limiting

Received: April 2, 2013
Accepted: June 3, 2013
Published: June 3, 2013

   dx.doi.org/10.1021/am4012066 | ACS Appl. Mater. Interfaces 2013, 5, 8881−8888

interferences (absorption, scattering, and autofluorescence) and thus a high signal-to-noise ratio.[21] Therefore, dyes emitting SSF in the NIR, particularly at above 650 nm, need to be further developed to provide advanced molecular nanoprobes for in vivo uses.

In the development of functional fluorescent dyes, combinatorial chemistry has been found to be a powerful methodology to reach the targeted goal.[22−25] However, this approach has rarely been utilized in developing SSF dye libraries for bioapplications. In this study, we present a combinatorial chemistry approach to discover dyes whose solid-state nanoaggregates emit in the NIR. First, we built a chemical library based on the dipolar arylvinyl (ArV) scaffold that is known to likely show SSF. To tune the SSF color toward the NIR, we attempted to control the intramolecular charge transfer (ICT) that stabilizes the electronic excited state to narrow the optical bandgap. To this end, the π-electron push-pull strengths were modulated by varying the donor and acceptor structures substituted at the scaffold. We then applied the library chemicals to bioimaging in cells and in vivo by formulating them into Pluronic (F-127)-encapsulated tiny molecular nanoprobes (FArV NPs) less than 20 nm. To prove the validity of our approach for biomedical in vivo imaging, we here demonstrate efficient lymph node imaging and tumor diagnosis with bright solid-state NIR fluorescence (NIRF) by injecting FArV NPs in mouse models.

RESULTS AND DISCUSSION

The structures and synthetic pathway of ArV are shown in Scheme 1. The dipolar arylvinyl scaffold was chosen for building the chemical library because it can be easily prepared through a modular synthesis in a combinatorial format[25] and some of the derivatives have been revealed to show efficient SSF.[26−28] The ArV structure is characterized by the dipolar π-conjugation having π-electron donor and acceptor at opposite ends. The compounds were synthesized by single-step Knoevenagel condensation between aromatic aldehyde donor (Ar−CHO) and active methylene (AM) acceptor building blocks. Aldehydes of aniline (An-CHO) and carbazole (Cb-CHO) were chosen as donor building blocks with different π-electron donating strengths. Ten acceptor building blocks were selected among active methylene compounds that contain one or two electron-accepting cyano or carbonyl substituents. The condensation was performed in ethanol in the presence of piperidine, and the precipitated products were purified by column chromatography. The hydrophobic products are soluble in common organic solvents but not in alcohols and water, which allows for the formation of solid-state nanoaggregates in physiological condition.

Semiempirical molecular orbital (MO) calculation demonstrated that all the dipolar ArV compounds have the ICT character clearly seen in the highest occupied molecular orbital (HOMO) and the lowest unoccupied molecular orbital (LUMO) diagrams; π-electrons are distributed around the donor in HOMO (reflecting the electronic ground state) but redistributed toward the acceptor in LUMO (reflecting the first excited state; see Figure S1 in the Supporting Information). The optimized geometries revealed that the bulky acceptors composed of α,α-disubstituted vinyl segment impose intramolecular steric hindrance and thus cause severe distortion, favorable for the occurrence of SSF. Indeed, it was found that all the obtained ArV compounds are fluorescent in solids, validating our molecular design strategy to obtain SSF (see Figure S2 in the Supporting Information).

The optical properties of ArV depending on the molecular state were comparatively studied in a good solvent (THF) and an aqueous poor solvent (THF/H_2O = 1/9 by vol.). In the latter aqueous milieu, hydrophobic ArV molecules precipitated into self-aggregated nanoparticles with a hydrodynamic size of ~50 nm (see Table S1 and Figure S3 in the Supporting Information). The results are summarized in Table 1 (for some representative spectra, see Figure S4 in the Supporting Information). As representatively shown in Figure 1, most of the ArV compounds exhibited the AEF behavior, i.e., weak fluorescence in solution and enhanced emission upon nanoaggregation. As suggested by the calculation results (see Figure S1 in the Supporting Information), the distorted π-conjugation of ArV can cause free twisting motion in the isolated solution state, leading to fast nonradiative decay and low fluorescence quantum yield.[7] Accordingly, the restricted quenching motion by aggregation can be a plausible reason for the AEF behavior. Upon aggregation, bathochromic alterations in the fluorescence spectra were observed, indicating that aggregation-induced planarization of the distorted geometry extends the effective π-conjugation length and thus narrows the optical bandgap. This suggests that the degree of planarization depending on the different molecular stacking mode of each ArV can affect the resulting SSF color of the formed nanoaggregates.

The dipolar ArV library with varying donor−acceptor combination manifested facile tunability of the SSF color, as summarized in Table 1. Importantly, the emission color covers a wide spectral range up to the NIR region (Figure 1). For the same acceptor units, aniline derivatives (AnV) showed red-shifted absorption and emission relative to the corresponding carbazole counterparts (CbV), confirming the fact that aniline is a stronger π-charge donor than carbazole. Compared to the loan pair electrons of nitrogen in aniline, those of carbazole are

Scheme 1. Structures and synthetic pathway of solid-state fluorescent dipolar arylvinyls (ArV)

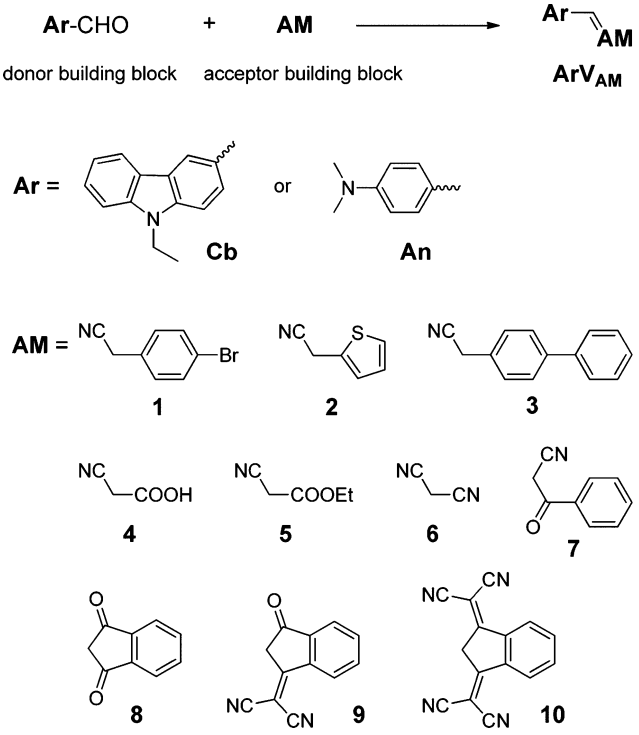

Table 1. Spectral properties of ArV in forms of solution, self-aggregates and polymer-encapsulated nanoparticles (FArV NPs)[a]

	solution (THF)			self-aggregates			FArV NPs				solution (THF)			self-aggregates			FArV NPs		
ArV	Abs (nm)	Em (nm)	QY (%)	Abs (nm)	Em (nm)	QY (%)	Abs (nm)	Em (nm)	QY (%)	ArV	Abs (nm)	Em (nm)	QY (%)	Abs (nm)	Em (nm)	QY (%)	Abs (nm)	Em (nm)	QY (%)
CbV1	369	452	0.23	387	500	2.23	380	460	3.5	**AnV1**	392	485	0.003	442	503	7.6	398	503	27.1
CbV2	370	447 548	0.26	397	530	2.94	383	465	3.6	**AnV2**	386	455 546	0.18	416	534	5.5	397	524	10.6
CbV3	386	465	0.41	394	519	6.5	383	470	6.3	**AnV3**	386	476	0.16	419	550	7.9	399	564	15
CbV4	388	458	0.49	370	506	2.2	372	482	2.6	**AnV4**	396	462	0.30	410	486	3.2	402	487	2.9
CbV5	394	460	0.37	432	510	22.9	398	470	12.3	**AnV5**	414	467	0.21	437	572	4.7	432	566	5.4
CbV6	405	472	0.29	421	513	12.1	466	536	40.3	**AnV6**	426	476	0.71	440	564	44	438	569	20
CbV7	406	486	0.32	437	546	8.7	424	548	7.5	**AnV7**	432	512	0.03	465	601	36	462	606	15.3
CbV8	448	510	0.23	460	630	15.2	440	624	14.7	**AnV8**	474	534	0.04	502	670	9.3	494	720	5.2
CbV9	513	574	0.61	562	740	19.8	550	732	18.2	**AnV9**	547	638	1.2	566	715	12.3	552	656	8.5
CbV10	580 630	654 705	12.6	584 624	661 709	15.8	582 633	658 708	18.7	**AnV10**	582 630	643 704	5.4	586 632	657 715	6.2	584 634	658 710	10.2

[a]Abs, absorption; Em, emission; QY, quantum yield; standard for QY, rhodamine B in ethanol. The ArV concentrations for all samples are 5 μM. Self-aggregates and FArV NPs were dispersed in THF/deionized water mixture (THF/H_2O = 1/9 v/v) and pure deionized water, respectively.

Figure 1. Representative photoluminescence (PL) spectra of ArV in solution (THF, dotted lines) and in dispersion of the self-aggregated nanoparticles (THF/deionized water = 1/9 v/v, solid lines) at 5 μM ((a) CbV5, (b) AnV1, (c) CbV7, (d) AnV7, (e) AnV8, (f) CbV9). (Insets) Fluorescence emission under 365 nm illumination. The NIR fluorescence image of CbV9 in f was taken by a Kodak imaging system with a filter set of excitation/emission for Cy5.5.

preferentially delocalized within the carbazole ring due to the additional aromatic stabilization, which hinders the charge transfer from the carbazole nitrogen toward the acceptor and thus lowers the extent of ICT, widening the optical bandgap.[29] Likewise, variations in the acceptor structure with a different number of acceptors with different accepting strength (cyano > ketone > ester) manifested a significant effect on the SSF color of the nanoaggregates. With one cyano group and a geminal aromatic ring attached to the vinyl end, CbV1−3 and AnV1−3 showed large bandgaps emitting blue-to-green SSF. The presence of two acceptors at the geminal vinyl end (CbV4−7 and AnV4−7) tuned the SSF color to the green-to-orange window. The SSF color could be further red-shifted by cyclic bridging of the two geminal acceptors with an additional phenyl ring, i.e., by using 1,3-indandione-based acceptors (CbV8−10 and AnV8−10). It is speculated that the phenyl bridge played a key role in the spectral red-shift by locking the two acceptors into an in-plane geometry as well as by extending the effective π-conjugation with additional aromaticity.[30] This speculation is supported by the calculation results for CbV8−10 and AnV8−10 (see Figure S1 in the Supporting Information), which demonstrated planar conformations of cyclic acceptors and the HOMO-to-LUMO π-electron redistribution up to the phenyl bridge end by ICT. With increasing the number of dicyanomethylidene substitution to the 1,3-indandione unit, the consequent SSF color approached to the true NIR (above 700 nm),

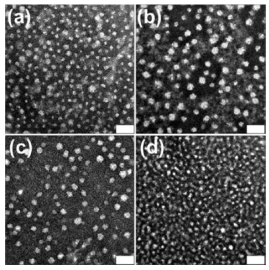

Figure 2. TEM images of FArV NPs of (a) CbV8 (6.3 ± 1.6 nm), (b) AnV8 (7.6 ± 2.2 nm), (c) CbV9 (7.2 ± 1.4 nm), and (d) CbV10 (6.1 ± 1.5 nm). Scale bars: 40 nm.

validating our combinatorial approach for tuning SSF to the NIR. Overall, our ArV library offers the SSF colors in the blue-to-NIR region, useful for a wide array of biological applications.

To apply the obtained SSF emission to bioimaging, dye-aggregated molecular nanoprobes (FArV NPs) were formulated by encapsulating ArV compounds with a biocompatible polymeric surfactant, Pluronic F-127. FArV NPs were prepared by solution mixing of ArV with Pluronic F-127 and adding water to the dried mixture. During the latter step, homogeneously dispersed colloids were spontaneously formed in water with no apparent precipitates being observed in the dispersion. Moreover, the hydrodynamic size of FArV NPs (less than 20 nm) were determined far smaller than those of ArV self-aggregates (seeTable S1 in the Supporting Information), suggesting that the water-insoluble ArV dyes were fully embedded in the hydrophobic interior of the self-assembled nanostructure of F-127. The transmission electron microscopic (TEM) images of representative NIR-emitting FArV NPs elucidated that the obtained colloids are spherical nanoparticles with average diameters less than 10 nm (Figure 2, for DLS size of all compounds see Figure S5 in the Supporting Information). The obtained colloidal sizes are small enough to facilitate circulation in the bloodstream and thus appropriate for in vivo applications of nanomaterials.[13,14] Figure 3 and Figure S4 demonstrate the blue-to-NIR fluorescence tunability of the resulting ArV-based molecular nanoprobes. Importantly, FArV NPs emitted the red-shifted and enhanced fluorescence in comparison to the corresponding solutions (Table 1). This implies that the ArV dyes are phase-separated and aggregated within the Pluronic nanoparticles to show the SSF emission, as observed in the self-aggregates.

The utility of FArV NPs for biomedical uses were demonstrated by performing fluorescence imaging experiments in cells and in vivo. For live cancer cell imaging, HeLa (human cervical epitheloid carcinoma) cells were incubated with FArV NPs. After 30 min of staining, the cytoplasmic regions displayed clear

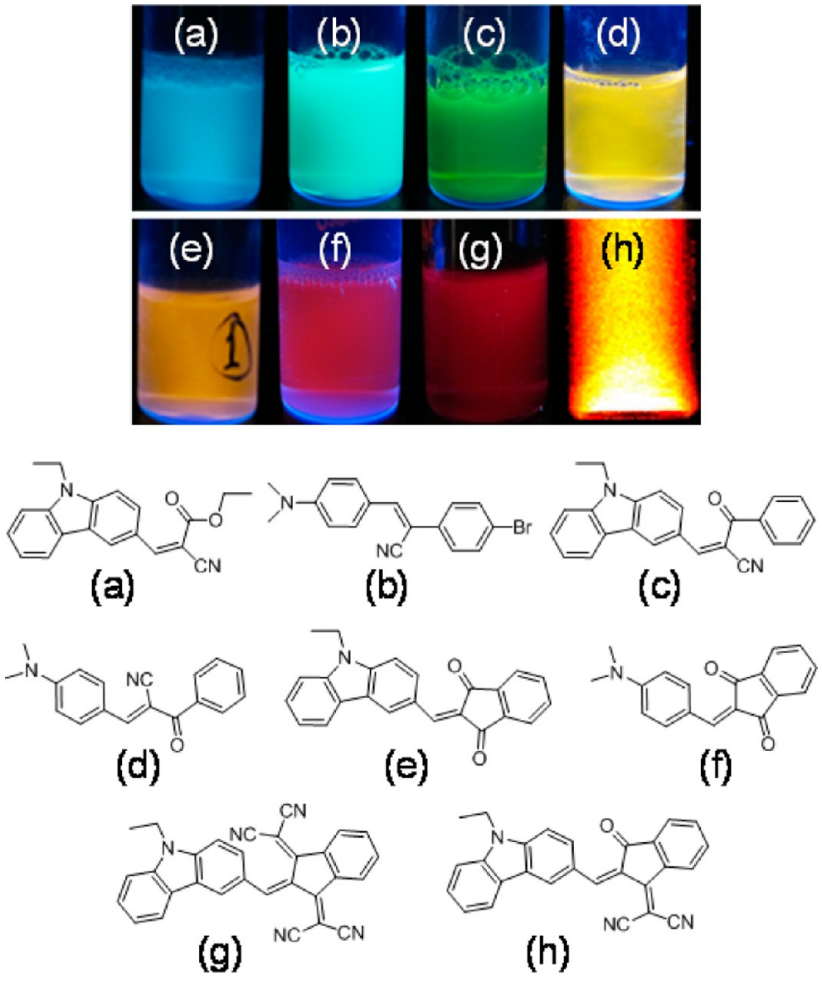

Figure 3. Fluorescence emission of representative FArV NPs under 365 nm illumination ((a) CbV5, (b) AnV1, (c) CbV7, (d) AnV7, (e) CbV8, (f) AnV8, (g) CbV10, (h) CbV9). The corresponding chemical structures of ArV are shown below. NIR fluorescence image of CbV9 (h) was taken by a Kodak imaging system with a filter set of excitation/emission for Cy5.5.

dx.doi.org/10.1021/am4012066 | ACS Appl. Mater. Interfaces 2013, 5, 8881−8888

multi-color fluorescence in the blue-to-NIR window, with the emission spectra of each nanoprobe well maintained in the intracellular environment (Figure 4). The efficient cellular

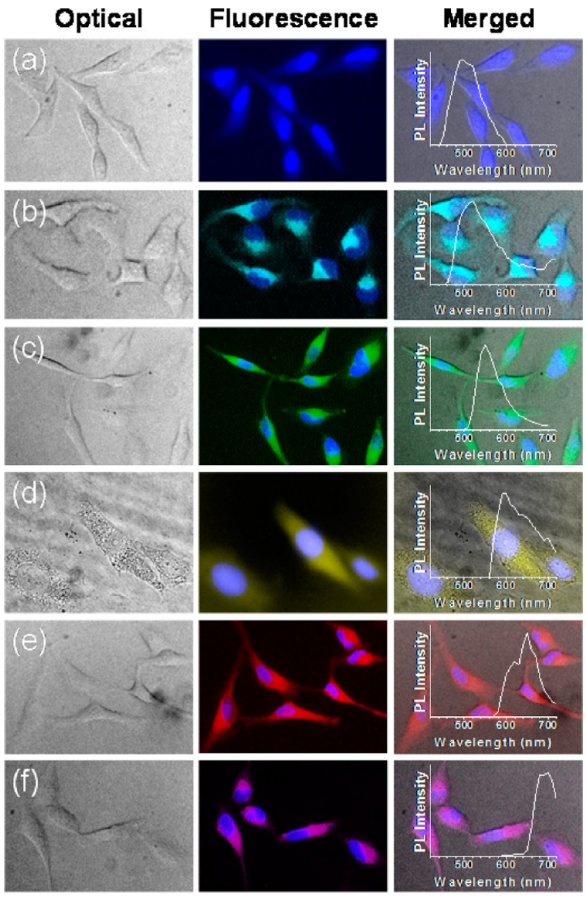

Figure 4. Optical, fluorescence and merged images of HeLa cells treated with FArV NPs of (a) CbV5, (b) AnV1, (c) CbV7, (d) AnV7, (e) AnV8, and (f) CbV9. Nuclei stained with DAPI are shown in blue. (Insets) Localized fluorescence spectra from the cytoplasmic regions.

uptake of FArV NPs is attributable to the surface characteristics of Pluronic nanoparticles that are known to promote several nondestructive endocytosis pathways.[31,32] Moreover, the Pluronic-surfaced nanoparticles showed minimal cytotoxicity under the imaging condition, probably due to the biocompatible surface nature and tiny colloidal size (see Figure S6 in the Supporting Information).

Prior to conducting in vivo imaging, the merit of employing NIR-SSF nanoparticles was evaluated in the in vivo-mimicking conditions. It is noted that the bright NIR-SSF emission from FAnV10 NPs and FCbV10 NPs (720−740 nm) could be taken by the far-red (or NIR) excitation at 640 nm, which offers an optimum condition for higher tissue penetration as well as to minimize autofluorescence background from biological tissues. This advantageous feature of NIR-excitable NIR-SSF was confirmed by measuring the signal-to-background (S/B) ratio through the thick biological specimen with huge autofluorescence (3.5 mm thick pork ham). For comparison, FArV NPs with different excitation/emission wavelength sets were employed and imaged with different excitation/emission filters: FCbV8 (430/620 nm; Vis./Vis.), FAnV8 (430/700 nm; Vis./NIR) and FCbV10 (640/720 nm; NIR/NIR). As demonstrated in Figure 5, the NIR/NIR combination for FCbV10 displayed the highest S/B

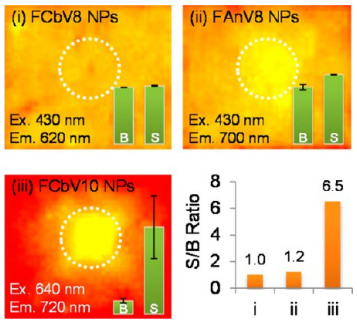

Figure 5. Quantification of fluorescence signals (S) from FArV NPs and the tissue autofluorescence background (B), along with the S/B ratio. Photoluminescence was excited and imaged through the biological tissue (3.5 mm thick pork ham, n = 3) with excitation (Ex.) and emission (Em.) filters whose wavelengths are given in the images. The signaling (S) areas are indicated with white circles.

ratio than the others because of the higher tissue penetration for both the excitation and emission lights. This observation verifies potential of SSF-emitting nanoparticles as bright NIRF probes useful for photon-limited and background-rich in vivo media. Moreover, it was found that the colloidal dispersion and optical properties of FCbV10 NPs were well maintained over time in 90% serum at 37 °C. No significant changes in fluorescence intensity and scattering were observed during serum incubation for 12 h, suggesting the chemical and colloidal stability in bodily fluid (see Figure S7 in the Supporting Information).

To demonstrate the in vivo imaging performance, FCbV10 NPs were injected intradermally into the forepaw pad of a mouse and applied to sentinel lymph node (SLN) mapping that is of clinical importance for cancer staging and surgery.[33] It was clearly imaged that a portion of the administered nanoprobes were accumulated at lymph nodes as early as five minutes post-injection (Figure 6a). In the ex vivo image, a typical NIR spectral signature of FAnV10 NPs was observed only in the two nodes (axillary and brachial) resected from the injection side (Figure 6b), indicating that the lymphatically drained nanoprobes were efficiently trapped in the SLNs. Rapid SLN mapping by the nanoprobes is attributable to their colloidal size (<20 nm) that is tiny enough for efficient lymphatic drainage and migration.[34] Importantly, FAnV10 NPs resulted in fairly high in vivo image contrast (S/B ratio = 8.2) with only a half reduction from the autofluorescence-free ex vivo value (16.5, Figure 6c), indicating that the bright NIR-SSF nanoprobes can delineate their tissue distribution with high accuracy.

The possible utility of bright NIR-SSF emission for disease imaging was elucidated with noninvasive whole-body visualization of mice bearing a visually undetectable subcutaneous small tumor by systemic administration. FCbV10 NPs were injected into the tail vein of BALB/c nude mice only 1 week after SCC7 cell inoculation and monitored under the NIR excitation/detection setting. As shown in Figure 7a, intense NIRF signals successfully display temporal tissue distribution of the blood-circulating nanoprobes. Importantly, a clear image contrast was seen at the tumor inoculation site within 10 min and increased up to 8 h post-injection, so as to readily locate the visually undetectable tumor. The spectral signatures evidenced that the strong tumor signal is indeed the fluorescence from FCbV10 NPs, confirming their accumulation at the tumor (Figure 7b). This behavior indicates the significant tumor accumulation of FCbV10 NPs thanks to the tiny colloidal size (<20 nm) and polyethylene glycol (PEG)-rich surface nature

dx.doi.org/10.1021/am4012066 | ACS Appl. Mater. Interfaces 2013, 5, 8881−8888

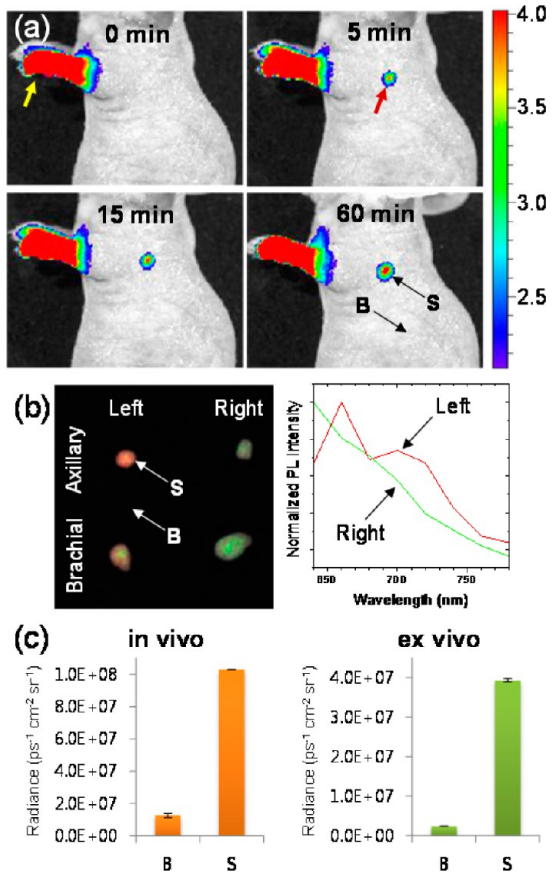

Figure 6. (a) NIRF images of a mouse (n = 5) injected intradermally with FCbV10 NPs into the left paw. Imaging time points after injection are shown. Yellow and red arrows indicate the injection site and a sentinel lymph node, respectively. (b) Pseudo-color ex vivo image. Lymph nodes resected from the injected (left) and the other (right) sides (shown in red and green, respectively) were spectrally unmixed according to their spectral profiles shown in the same colors (right). (c) In vivo and ex vivo intensities of FCbV10 NPs in the areas of signal (S) and background (B) indicated in a and b.

of the Pluronic nanoparticles. These attributes can reduce the clearance of nanomaterials by the reticulo-endothelial system (RES) and thus prolong the circulation in the bloodstream, facilitating their passive tumor targeting via the size-motivated EPR effect.[13,14] The ex vivo image of resected organs indicates the nanoprobe accumulation mainly in the tumor whose fluorescence signal is stronger than those from other organs (see Figure S8 in the Supporting Information). The in vivo image contrast was found to be fairly high (S/B ratio = 7.9, Figure 7c), as in the case of SLN imaging. Overall, these imaging results demonstrate the potential of NIR-SSF nanoprobes to detect and diagnose tumors at a very early stage of their development owing to the efficient tumor target ability as well as the high image contrast by intense fluorescence signal in the tissue-transparent NIR region.

CONCLUSION

We have applied a combinatorial chemistry approach using a dipolar arylvinyl (ArV) scaffold to discover dyes whose nanoaggregates emit in the NIR. Through the combinatorial modulation of the degree of ICT, the solid-state fluorescence (SSF) of ArV was successfully tuned to the NIR above 700 nm. The obtained ArV compounds could be stably formulated into a Pluronic-based biocompatible nanoparticles (FArV NPs) that are smaller than 20 nm and cell-permeable with minimal cytotoxicity. It turned out that the NIR-SSF from some of FArV NPs displayed a high signal-to-background ratio (S/B ≈ 8) in the autofluorescence-rich in vivo conditions due to their truly NIR excitation and emission wavelengths, both of which coincide with the biologically transparent optical window. Efficient NIR excitation and emission of SSF as well as facile circulation in the living body allowed for high-contrast and noninvasive in vivo imaging of SLN and visibly undetectable tumor in its early phase of growth, validating our combinatorial chemistry strategy to construct the SSF-based advanced nanoprobes for biomedical imaging applications.

EXPERIMENTAL SECTION

Materials and Instrumentation. All chemical reagents were purchased from Aldrich and TCI and used as received. Chemical structures were identified by FT-IR (Thermo Mattsonmodel Infinity Gold FT-IR), ^{1}H NMR (Varian unity plus 300) and elemental analysis performed on a CHNS analyzer (EA 1180, FISONS Instruments). Particle size distribution of nanoparticle dispersion in deionized water was determined at 25 °C by using a zeta-sizer (Nano-ZS, Malvern). Transmission electron microscopic (TEM) images were obtained with a CM30 electron microscope (FEI/Philips) operated at 200 kV. For the TEM sample preparation, a drop of particle dispersion was dried on a 300-mesh copper grid coated with carbon and negatively stained with a 2 wt % uranyl acetate solution. From the TEM images, 60 particles were counted for the size analysis of each sample. Absorption and emission spectra were acquired using a UV-visible spectrometer (Agilent 8453) and a fluorescence spectrophotometer (Hitachi F-7000,

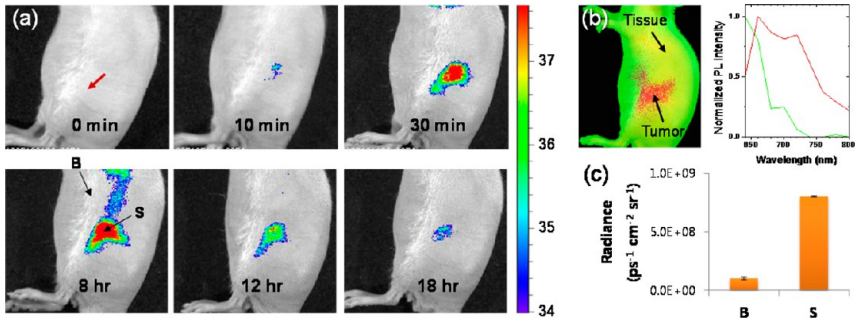

Figure 7. (a) NIRF images of a mouse (n = 5) injected with FCbV10 NPs into the tail vein. Imaging time points after injection are shown. Invisible subcutaneous SCC7 tumor in its early phase of growth (1 week post-inoculation) is indicated with a red arrow. (b) Pseudo-color in vivo image taken at 12 h post-injection (left). Tissue autofluorescence (green) and FCbV10 NPs signal (red) were spectrally unmixed according to their spectral profiles shown in the same colors (right). (c) In vivo intensities of FCbV10 NPs in the areas of signal (S) and background (B) indicated in a.

dx.doi.org/10.1021/am4012066 | ACS Appl. Mater. Interfaces 2013, 5, 8881−8888

wavelength calibrated for excitation and emission), respectively. Relative fluorescence quantum yields (Φf) were determined using an ethanol solution of rhodamine B as a reference.

General Procedure for ArV Synthesis. All ArV compounds were synthesized by Knoevenagel condensation depicted in Scheme 1. Typically, a solution of the aromatic aldehyde donor (**Ar**-CHO, 1.0 mmol) and active methylene acceptor (**AM**, 1.0 mmol) in absolute EtOH (10 mL) was treated portion wise with piperidine (0.1 mmol) and stirred at 60 °C for 2−3 h. After cooling to 0 °C, the precipitate was filtered and washed with chilled EtOH. The dried crude product was purified by column chromatography on silica gel using chloroform as an eluent to give a pure solid. The characterization data for all compounds are provided in the Supporting Information.

Preparation of ArV Self-Aggregates. Aqueous dispersions of ArV nanoaggregates were prepared without surfactant for the study of their AEF behaviors. Briefly, THF stock solution of each ArV compound (50 μM, 1 mL) was added by one shot to 9 mL of deionized water under sonication, to have the final ArV concentration of 5 μM. For comparative study, THF solutions of the same concentration were prepared by mixing the THF stock solution (50 μM, 1 mL) with 9 mL of THF.

Preparation of FArV NPs. For all ArV compounds, polymer-encapsulated nanoparticles of dye aggregates were prepared with Pluronic F-127 surfactant for in vitro and in vivo imaging. Typically, a mixture of F-127 (20 mg) and ArV (0.3 mg) was dissolved in 1 mL of THF. After solvent evaporation by air blowing, the dried mixture was mixed with 2 mL of deionized water and agitated under a few seconds of sonication, to afford clear aqueous dispersion of hydrophobic dye aggregates with the ArV concentration of 150 μg/mL.

In Vitro Cell Labeling and Imaging. HeLa cells were cultured in Dulbecco's modified Eagle medium with 10% FBS, 5 mM L-glutamine, and 5 μg/mL gentamicin in a humidified 5% CO_2 incubator at 37 °C. Cells were seeded onto 35 mm cover glass bottom dishes and allowed to grow until a confluence of 70%. Prior to experiments, cells were washed twice with PBS (pH 7.4) to remove the remnant growth medium and then incubated in a serum-free medium (1.8 mL) containing FArV NPs (200 μL) for 30 min. For photoluminescence imaging, the labeled cells were then washed twice with PBS (pH 7.4) and directly imaged using a LEICA DMI3000B equipped with a Nuance FX multispectral imaging system (CRI, USA).

In Vivo Sentinel Lymph Node and Tumor Imaging. The animal studies have been approved by the animal care and use committee of Korea Institute of Science and Technology, and all handling of mice was performed in accordance with the institutional regulations. For tumor model preparation, SCC7 cell line was injected in BALB/c mice (male, 5 weeks of age; Orient Bio Inc., Korea). Mice were anaesthetized with intraperitoneal injection of 0.5% pentobarbital sodium (0.01 mL/g) before experiments. For sentinel lymph node imaging, 20 μL of FCbV10 NPs were injected into forepaw pad of normal mice, and for tumor imaging, 200 μL of FCbV10 NPs were injected intravenously into the tail vein of tumor-bearing mice. In vivo imaging was done with an IVIS Spectrum imaging system (Caliper, USA).

■ ASSOCIATED CONTENT

Ⓢ Supporting Information

Characterization data for the ArV synthesis, supplementary figures, and table. This material is available free of charge via the Internet at http://pubs.acs.org.

■ AUTHOR INFORMATION

Corresponding Author

*E-mail: sehoonkim@kist.re.kr (S.K.); ccdjko@konkuk.ac.kr (J.K.).

Author Contributions

§Authors A.S. and C.-K.L. contributed equally to this work.

Notes

The authors declare no competing financial interest.

■ ACKNOWLEDGMENTS

This work was supported by the Pioneer Program and MD-PhD Program through the National Research Foundation of Korea funded by the Ministry of Science, ICT & Future Planning (Nos. 2012-0001082 and 2012-0006061), and by the Intramural Research Program of KIST (2V03110).

■ REFERENCES

(1) Weissleder, R.; Ntziachristos, N. *Nat. Med.* **2003**, *9*, 123−128.
(2) Haugland, R. P. *Handbook of Fluorescent Probes and Research Products*, 9th ed.; Molecular Probes Inc.: Eugene, OR, 2002.
(3) Tong, H.; Hong, Y.; Dong, Y.; Häußler, M.; Lam, J. W. Y.; Li, Z.; Guo, Z.; Guo, Z.; Tang, B. Z. *Chem. Commun.* **2006**, 3705−3707.
(4) Kim, H.-J.; Lee, J.; Kim, T.-H.; Lee, T. S.; Kim, J. *Adv. Mater.* **2008**, *20*, 1117−1121.
(5) Kim, S.; Pudavar, H. E.; Bonoiu, A.; Prasad, P. N. *Adv. Mater.* **2007**, *19*, 3791−3795.
(6) Kim, S.; Huang, H.; Pudavar, H. E.; Cui, Y.; Prasad, P. N. *Chem. Mater.* **2007**, *19*, 5650−5656.
(7) Lim, C. K.; Kim, S.; Kwon, I.C.; Ahn, C. H.; Park, S. Y. *Chem. Mater.* **2009**, *21*, 5819−5825.
(8) Lee, YD.; Lim, CK.; Singh, A.; Koh, J.; Kim, J.; Kwon, IC.; Kim, S. *ACS Nano* **2012**, *6*, 6759−6766.
(9) Kim, S.; Lim, C.K.; Na, J.; Lee, Y. D.; Kim, K.; Choi, K.; Leary, J. F.; Kwon, I. C. *Chem. Commun.* **2010**, *46*, 1617−1619.
(10) Wang, X.; Morales, A. R.; Urakami, T.; Zhang, L.; Bondar, M. V.; Komatsu, M.; Belfield, K. D. *Bioconjugate Chem.* **2011**, *22*, 1438−1450.
(11) Qin, W.; Ding, D.; Liu, J.; Yuan, W. Z.; Hu, Y.; Liu, B.; Tang, B. Z. *Adv. Funct. Mater.* **2012**, *22*, 771−779.
(12) Zhao, Q.; Li, K.; Chen, S.; Qin, A.; Ding, D.; Zhang, S.; Liu, Y.; Liu, B.; Sun, J. Z.; Tang, B. Z. J. *Mater. Chem.* **2012**, *22*, 15128−15135.
(13) Albanese, A.; Tang, P. S.; Chan, W. C.W. *Annu. Rev. Biomed. Eng.* **2012**, *14*, 1−16.
(14) Schadlich, A.; Caysa, H.; Mueller, T.; Tenambergen, F.; Rose, C.; Gopferich, A.; Kuntsche, J.; Mader, K. *ACS Nano* **2011**, *5*, 8710−8720.
(15) Luo, J.; Xie, Z.; Lam, J. W. Y.; Cheng, L.; Chen, H.; Qiu, C.; Kwok, H. S.; Zhan, X.; Liu, Y.; Zhu, D.; Tang, B. Z. *Chem. Commun.* **2001**, 1740−1741.
(16) Hong, Y.; Lam, J. W. Y.; Tang, B. Z. *Chem. Commun.* **2009**, 4332−4353.
(17) An, B.-K.; Kwon, S.-K.; Jung, S.-D.; Park, S. Y. J. *Am. Chem. Soc.* **2002**, *124*, 14410−14415.
(18) An, B.K.; Gierschner, J.; Park, S. Y. *Acc. Chem. Res.* **2012**, *45*, 544−554.
(19) Kim, S.; Zheng, Q.; He, G. S.; Bharali, D. J.; Pudavar, H. E.; Baev, A.; Prasad, P. N. *Adv. Funct. Mater.* **2006**, *16*, 2317−2323.
(20) Shimizu, M.; Takeda, Y.; Higashi, M.; Hiyama, T. *Angew. Chem., Int.Ed.* **2009**, *48*, 3653−3656.
(21) Prasad, P. N. *Introduction to Biophotonics*; John Wiley & Sons: Hoboken, NJ, 2003.
(22) Kim, E.; Koh, M.; Ryu, J.; Park, S. B. J. *Am. Chem. Soc.* **2008**, *130*, 12206−12207.
(23) Vendrell, M.; Zhai, D.; Er, J. C.; Chang, Y. T. *Chem. Rev.* **2012**, *112*, 4391−4420.
(24) Wang, S.; Chang, Y. T. J. *Am. Chem. Soc.* **2006**, *128*, 10380−10381.
(25) Ryabukhin, S. V.; Plaskon, A. S.; Volochnyuk, D. M.; Pipko, S. E.; Shivanyuk, A. N.; Tolmachev, A. A. *J. Comb. Chem.* **2007**, *9*, 1073−1078.
(26) Ning, Z.; Chen, Z.; Zhang, Q.; Yan, Y.; Qian, S.; Cao, Y.; Tian, H. *Adv. Funct. Mater.* **2007**, *17*, 3799−3807.
(27) Ishow, E.; Brosseau, A.; Clavier, G.; Nakatani, K.; Tauc, P.; Fiorini-Debuisschert, C.; Neveu, S.; Sandre, O.; Léaustic, A. *Chem. Mater.* **2008**, *20*, 6597−6599.
(28) Zhang, X.; Loh, K. P.; Sullivan, M. B.; Chen, Z. K.; Liu, M. *Cryst. Growth Des.* **2008**, *8*, 2543−2546.

(29) Ryu, H.; Subramanian, L. R.; Hanack, M. *Tetrahedron* **2006**, *62*, 6236−6247.
(30) Heo, J.; Lim, C.-K.; Whang, D. R.; Shin, J.; Jeong, S. Y.; Park, S. Y.; Kwon, I. C.; Kim, S. *Chem.—Eur. J.* **2012**, *18*, 8699−8704.
(31) Muniruzzaman, M.; Marin, A.; Luo, Y.; Prestwich, G. D.; Pitt, W. G.; Husseini, G.; Rapoport, N. Y. *Colloids Surf., B* **2002**, *25*, 233−241.
(32) Mei, L.; Zhang, Y.; Zheng, Y.; Tian, G.; Song, C.; Yang, D.; Chen, H.; Sun, H.; Tian, Y.; Liu, K.; Li, Z.; Huang, L. *Nanoscale Res. Lett.* **2009**, *4*, 1530−1539.
(33) Jakub, J. W.; Pendas, S.; Reintgen, D. S. *Oncologist* **2003**, *8*, 59−68.
(34) Moghimi, S. M.; Rajabi-Siahboomi, A. R. *Prog. Biophys. Mol. Biol.* **1996**, *65*, 221−249.